Line Tension and Contact Angle of Heterogeneous Nucleation of Binary Fluids

Di Zhou, Fangfang Zhang, Jianguo Mi, and Chongli Zhong
State Key Laboratory of Organic-Inorganic Composites, Department of Chemical Engineering, Beijing University of Chemical Technology, Beijing 100029, China

DOI 10.1002/aic.14159
Published online June 21, 2013 in Wiley Online Library (wileyonlinelibrary.com)

Due to its complexity, line tension is usually neglected or indirectly estimated in studying heterogeneous nucleation. In this work, we try to provide a direct and quantitative description of it. Within a three-dimensional density functional framework, the total excess free energy and individual energies at different two-phase interfaces are calculated during the droplet or bubble nucleation in binary fluids, and the line tension and contact angle are determined simultaneously. Meanwhile, the contact angle can also be measured directly from the spatial configuration of droplet or bubble. Comparing the calculated and measured contact angles, one can see that a good agreement is achieved for bubble and droplet at solvophilic and solvophobic walls. It is shown that line tension provides a considerable modification of contact angle prediction that is of great importance in engineering applications. © 2013 American Institute of Chemical Engineers *AIChE J*, 59: 4390–4398, 2013

Keywords: excess free energy, line tension, contact angle, Tolman length, heterogeneity

Introduction

Nucleation accompanying first-order phase transition is a topic of wide interest in many scientific studies and technological processes.[1,2] Due to the strict requirements for sample purity and experimental conditions,[3–5] most nucleation occurs heterogeneously in nature.[6–12] Heterogeneous nucleation usually occurs in the presence of foreign objects, such as on solid surfaces[6–10] or suspended seed particles.[11,12] At present, theoretical interpretation of heterogeneous nucleation is still immature.

For heterogeneous nucleation, the energy of formation of a new phase includes not only the excess free energies at the liquid−solid, vapor−solid, and vapor−liquid interfaces but also the energy at the three-phase contact line. In classical heterogeneous nucleation theory, the total free energy is represented with homogeneous nucleation free energy multiplied by a function of the contact angle.[13] The theory cannot accurately describe the thermodynamic properties of heterogeneous nucleation, as the two-phase interfacial free energies are independent of the supersaturated condition, and the total energy is calculated without considering the microstructure of nucleus. As such, the intercorrelation of different interfacial free energies was disregarded.

In fact, at three-phase contact line, there exists line tension, which is defined as the difference per unit length of the contact line between the actual interfacial energy of the system and the individual interfacial energies. It is known that line tension plays an important role in multiphase systems, such as froth flotation,[14] petrochemical industry,[15] and dropwise condensation heat transfer.[16] Similarly, nucleation process is also sensitive to line tension effects.[17] A multitude of previous studies focused on this subject.[18–20] However, there is little consensus about the magnitude and sign of line tension.

Experimentally, line tension is obtained indirectly by the measured contact angle with appropriate thermodynamic correlation.[21–23] Most of these experiments rely on optical microscopes to deduce the contact angle from geometric measurements. To date, the accurate experimental measurement of the line tension is still a big challenge.

Theoretically, Marmur et al.[24,25] constructed an approximate equation to deal with the line tension as well as the contact angle of liquid drops on nanospheres. Widom and coworkers[26,27] provided a geometric interpretation of adsorption at the three-phase contact line and conjectured a line adsorption equation. Schimmele and Napiorkowski[28] found two different definitions of line tension in case of a droplet in contact with a gas on a solid substrate. Indekeu et al.[29] discussed the contribution of the core structure to the line tension near a wetting transition. In our previous investigations,[30,31] the influence of line tension on the wetting behavior of spherical nanoparticles at a vapor–liquid interface was analyzed. These works show clearly that line tension is non-neglectable.

Very recently, we have presented a three dimensional density functional theory (3D DFT) approach to describe heterogeneous nucleation of pure Lennard-Jones (LJ) fluid.[32] This work has shown good prospective of the theoretical model in description of heterogeneous nucleation. In this contribution, the 3D DFT approach is extended to study the growing droplet and bubble of binary fluid mixture on solvophilic and solvophobic walls. The line tension and contact angle are our main concern. For the numerical solution algorithm in 3-D

Correspondence concerning this article should be addressed to J. Mi at mijg@mail.buct.edu.cn.

systems, fast Fourier tranform to evaluate the convolution of the Euler-Lagrange equation and Picard (iterative substitution) iteration with line search are used. The algorithm can extensively save computational time and memory usage.[33] To analyze line tension and contact angle, the density and excess free energy distributions of droplets and bubbles on different walls are calculated and presented in details. Accordingly, the individual interfacial free energies and total excess free energy are quantitatively determined. As a result, the line tension and contact angle are derived out based on these energies. Unlike classic heterogeneous nucleation theory, the current theory ensures the individual and total excess free energy calculations within the same 3-D space. Another important product of the theory is that the contact angle can be measured directly based on the droplet (bubble) configuration. By comparing the measured contact angle with the calculated one, the accuracy of 3-D-DFT can be validated. In addition, Tolman lengths for the correlation of curvature interface tensions and planar interface tensions of droplet and bubble are analyzed.

Theory

3-D-DFT for LJ fluid mixture

For LJ mixtures, molecules interact through the potential

$$u_{ij}(r)=4\varepsilon_{ij}\left[\left(\frac{\sigma_{ij}}{r}\right)^{12}-\left(\frac{\sigma_{ij}}{r}\right)^{6}\right] \tag{1}$$

where ε_{ij} and σ_{ij} are the LJ energy and length parameters, respectively. Interaction parameters are calculated using the Lorentz–Berthelot mixing rules

$$\sigma_{ij}=\frac{\sigma_{ii}+\sigma_{jj}}{2} \tag{2}$$

$$\varepsilon_{ij}=\sqrt{\varepsilon_{ii}\varepsilon_{jj}} \tag{3}$$

For a binary mixture, the grand potential of the system, $\Omega[\rho_1(\mathbf{r}),\rho_2(\mathbf{r})]$, can be expressed as

$$\Omega[\rho_1(\mathbf{r}),\rho_2(\mathbf{r})]=F[\rho_1(\mathbf{r}),\rho_2(\mathbf{r})]+k_BT\sum_{i=1}^{2}\int\rho_i(\mathbf{r})\left(V_i^{\text{ext}}(\mathbf{r})-\mu_i\right)d\mathbf{r} \tag{4}$$

where $F[\rho_1(\mathbf{r}),\rho_2(\mathbf{r})]$ indicates the intrinsic Helmholtz free energy, μ_i stands for the bulk chemical potential of component i and $V_i^{\text{ext}}(\mathbf{r})$ indicates the external force affecting component i, which only depends on z-direction and can be given by[34]

$$V_i^{\text{ext}}(z)=2\pi\varepsilon_{i\text{w}}\sigma_{i\text{w}}^2\left[\frac{2}{5}\left(\frac{\sigma_{i\text{w}}}{z}\right)^{10}-\left(\frac{\sigma_{i\text{w}}}{z}\right)^{4}\right] \tag{5}$$

in which $\varepsilon_{i\text{w}}$ and $\sigma_{i\text{w}}$ are the LJ parameters between component i and wall, and can be obtained from Eqs. 2 and 3.

The intrinsic Helmholtz free energy of the mixture $F[\rho_1(\mathbf{r}),\rho_2(\mathbf{r})]$ includes the ideal, hard-sphere repulsion and dispersion attraction parts. The ideal part is given by

$$F^{\text{id}}[\rho_1(\mathbf{r}),\rho_2(\mathbf{r})]=k_BT\sum_{i=1}^{2}\int\rho_i(\mathbf{r})\left[\ln\left(\rho_i(\mathbf{r})\Lambda_i^3\right)-1\right]d\mathbf{r} \tag{6}$$

with k_B the Boltzmann constant and Λ_i the de Broglie wavelength of component i.

According to the modified fundamental measure theory,[35] the hard-sphere repulsion part can be expressed as

$$F^{\text{rep}}[\rho_1(\mathbf{r}),\rho_2(\mathbf{r})]=k_BT\int\Phi^{\text{hs}}[n_\alpha(\mathbf{r})]d\mathbf{r} \tag{7}$$

with

$$\Phi^{\text{hs}}[n_\alpha(\mathbf{r})]=-n_0\ln(1-n_3)+\frac{n_1n_2-\mathbf{n}_{V1}\cdot\mathbf{n}_{V2}}{1-n_3}+\frac{1}{36\pi}\times\left(n_3\ln(1-n_3)+\frac{n_3^2}{(1-n_3)^2}\right)\frac{n_2^3-3n_2\mathbf{n}_{V2}\cdot\mathbf{n}_{V2}}{n_3^3} \tag{8}$$

In 3-D-DFT, the weighted densities n_α can be computed using the fast Fourier transform

$$n_\alpha(\mathbf{r})=\sum_{i=1}^{2}\int\rho_i\left(\mathbf{r}'\right)w_i^{(\alpha)}\left(\mathbf{r}-\mathbf{r}'\right)d\mathbf{r}'=\mathcal{F}^{-1}\left(\tilde{\rho}_i(\mathbf{k})\cdot\tilde{w}_i{}^{(\alpha)}(\mathbf{k})\right) \tag{9}$$

in which $\mathcal{F}$ stands for the Fourier transform operator, and the tilde notation means the Fourier image of the function. The weight functions $\tilde{w}_i{}^{(\alpha)}(\mathbf{k}),\alpha=0,1,2,3,V1,V2$ are given by[33]

$$\tilde{w}_i{}^{(2)}(\mathbf{k})=\pi d_i^2\tilde{w}_i{}^{(0)}(\mathbf{k})=2\pi d_i\tilde{w}_i{}^{(1)}(\mathbf{k})=2\pi d_i\sin(kd_i/2)/k \tag{10}$$

$$\tilde{w}_i{}^{(3)}(\mathbf{k})=\frac{4\pi}{k^3}(\sin(kd_i/2)-(kd_i/2)\cos(kd_i/2)) \tag{11}$$

$$\tilde{w}_i{}^{(V2)}(\mathbf{k})=2\pi d_i\tilde{w}_i{}^{(V1)}(\mathbf{k})=\frac{-4\pi\imath}{k^3}\times(\sin(kd_i/2)-(kd_i/2)\cos(kd_i/2))\mathbf{k} \tag{12}$$

Here, d_i is the Barker–Henderson diameter.[36]

Using the weighted density approximation,[37] the dispersion attraction part can be written as

$$F^{\text{att}}[\rho_1(\mathbf{r}),\rho_2(\mathbf{r})]=k_BT\sum_{i=1}^{2}\int\rho_i(\mathbf{r})\{a[\bar{\rho}_i(\mathbf{r})]\}d\mathbf{r} \tag{13}$$

in which $a[\bar{\rho}_i(\mathbf{r})]$ can be expressed by[38]

$$a[\bar{\rho}_i(\mathbf{r})]=-2\pi\bar{\rho}_i(\mathbf{r})\beta\sum_i\sum_j x_ix_j\varepsilon_{ij}\left[k_{1,ij}\left(G_{0,ij}\left(z_{1,ij}\right)e^{z_{1,ij}R_{ij}}-\frac{1+z_{1,ij}R_{ij}}{z_{1,ij}^2}\right)-k_{2,ij}\left(G_{0,ij}\left(z_{2,ij}\right)e^{z_{2,ij}R_{ij}}-\frac{1+z_{2,ij}R_{ij}}{z_{2,ij}^2}\right)\right]+8\pi\bar{\rho}_i(\mathbf{r})\beta\sum_i\sum_j x_ix_j\varepsilon_iR_{ij}^3I_i-8\pi\bar{\rho}_i(\mathbf{r})\beta\sum_i\sum_j x_ix_j\varepsilon_ig_0(R_i)R_{ij}^3I_{ij,1} \tag{14}$$

with

$$I_{ij,\infty}=\frac{1}{9}\left(\frac{\sigma_{ij}}{R_{ij}}\right)^{12}-\frac{1}{3}\left(\frac{\sigma_{ij}}{R_{ij}}\right)^{6} \tag{15}$$

$$I_{ij,1}=\frac{1}{9}\left(\frac{\sigma_{ij}}{R_{ij}}\right)^{12}-\frac{1}{3}\left(\frac{\sigma_{ij}}{R_{ij}}\right)^{6}+\frac{2}{9}\left(\frac{\sigma_{ij}}{R_{ij}}\right)^{3} \tag{16}$$

The more details of Eq. 14 can be seen in Ref. 38. $\bar{\rho}_i(\mathbf{r})$ is the weighted density

$$\bar{\rho}_i(\mathbf{r})=\sum_{j=1}^{2}\int \rho_j(\mathbf{r}')\omega_{ij}^{\mathrm{att}}(|\mathbf{r}-\mathbf{r}'|)d\mathbf{r}' \tag{17}$$

where $\omega_{ij}^{\mathrm{att}}(r)$ is the weight function

$$\omega_{ij}^{\mathrm{att}}(r)=\frac{c_{ij}^{\mathrm{att}}(r)}{\int c_{ij}^{\mathrm{att}}(r)d\mathbf{r}} \tag{18}$$

in which $c_{ij}^{\mathrm{att}}(r)$ is the attractive part of direct correlation function.[39] In two-phase coexistence system, it is calculated from the equilibrium interfacial density, that is, $(\rho_l+\rho_v)/2$.

In 3-D space, the $\bar{\rho}_i(\mathbf{r})$ integrals (Eq. 17) can be evaluated by the fast Fourier transform

$$\bar{\rho}_i(\mathbf{r})=\sum_{j=1}^{2}\int \rho_j(\mathbf{r}')\omega_{ij}^{\mathrm{att}}(|\mathbf{r}-\mathbf{r}'|)d\mathbf{r}'=F^{-1}\left(\tilde{\rho}_j(\mathbf{k})\cdot\tilde{\omega}_{ij}^{\mathrm{att}}(\mathbf{k})\right) \tag{19}$$

By minimizing the grand potential Eq. 4 and solving the Euler–Lagrange equation, the 3-D equilibrium density distribution of component i can be obtained by

$$\rho_i(\mathbf{r})=\rho_i^{\mathrm{b}}\exp\left\{\beta\mu_i^{\mathrm{ex}}-\beta\frac{\delta F^{\mathrm{rep}}[\rho_1(\mathbf{r}),\rho_2(\mathbf{r})]}{\delta\rho_i(\mathbf{r})}-\beta\frac{\delta F^{\mathrm{att}}[\rho_1(\mathbf{r}),\rho_2(\mathbf{r})]}{\delta\rho_i(\mathbf{r})}-\beta V_i^{\mathrm{ext}}(\mathbf{r})\right\} \tag{20}$$

Here, $\beta=1/k_{\mathrm{B}}T$, ρ_i^{b}, and μ_i^{ex} are, respectively, the density and excess chemical potential of component i in bulk phase.

For 3-D-DFT calculation, the Cartesian coordinate is adopted, and the system is discretized into $256\times256\times256$ grids with the grid spacing $0.1\sigma_1$ in each axis. By consideration of the boundary effect, the position of solid walls is all set at $z_0=3\sigma_1$. Accordingly, Eq. 20 can be solved using Picard iterations. The iteration procedure is repeated until the average fractional difference over any 3-D grid point between the old and the new 3-D density function is less than10^{-4}.

Once the equilibrium density distributions of binary mixture have been obtained, the corresponding excess free energy distributions

$$\beta\Delta F(\mathbf{r})=\sum_{i=1}^{2}\rho_i(\mathbf{r})\left[\ln\left(\rho_i(\mathbf{r})\Lambda_i^3\right)-1\right]+\Phi^{\mathrm{hs}}[n_\alpha(\mathbf{r})]+\sum_{i=1}^{2}\rho_i(\mathbf{r})\{a[\bar{\rho}_i(\mathbf{r})]\}+\sum_{i=1}^{2}\rho_i(\mathbf{r})\left(V_i^{\mathrm{ext}}(\mathbf{r})-\mu_i\right) \tag{21}$$

can be determined for the following line tension and contact angle calculation.

Nucleation energy barrier

Nucleation normally occurs under a supersaturated condition. For nucleation of pure fluid, droplets (bubbles) can emerge in the environment of supersaturated vapor (liquid), and the supersaturation ratio is defined as $S=p/p^0$, where p denotes the pressure of the supersaturated vapor (liquid) and p^0 means the vapor–liquid coexistence pressure at a fixed temperature. For droplet (bubble) nucleation of binary mixture, the supersaturation can be induced either by the excessive supersaturation of component i in vapor (liquid) phase or by the variation of pressure at a certain temperature. In this work, we take into account the former case, and the supersaturation ratio is defined as the ratio of the enriched density of component i to its bulk density in the corresponding phase $S=\rho_i/\rho_i^{\mathrm{b}}$.

In the growing process of droplet (bubble), the constrained free energy can be calculated by

$$\Delta\Omega=\Omega[\rho_1(\mathbf{r}),\rho_2(\mathbf{r})]-\Omega_{\mathrm{b}} \tag{22}$$

in which Ω_{b} is the grand potential of the external bulk fluid in contact with the substrate.

Line tension

In consideration of the effect of line tension on heterogeneous nucleation, modified Young's equation on a solid wall can be expressed as[40]

$$\gamma_{\mathrm{vw}}-\gamma_{\mathrm{lw}}-\gamma_{\mathrm{vl}}\cos\theta-\frac{\tau}{R\sin\theta}=0 \tag{23}$$

for droplet and

$$\gamma_{\mathrm{lw}}-\gamma_{\mathrm{vw}}-\gamma_{\mathrm{vl}}\cos\theta-\frac{\tau}{R\sin\theta}=0 \tag{24}$$

for bubble. In this work, the contact angle θ is specified as that measured from the inside of droplet or bubble. The three interfacial tensions, vapor–liquid tension γ_{vl}, vapor–wall tension γ_{vw}, and liquid–wall tension γ_{lw} can be obtained through

$$\gamma=\frac{\Delta\Omega}{A}=\frac{\Omega+pV}{A} \tag{25}$$

where Ω can be obtained from Eq. 4 based on the 3-D density profile at the two-phase interface, V is the volume of the system, A is the interfacial area.

Besides above Eq. 23 or 24, another free energy equilibrium equation needs to be satisfied. Following Marmur's analysis,[25,26] it can be written as

$$\tau\ 2\pi R\sin\theta=\Delta\Omega-(\gamma_{\mathrm{vl}}A_{\mathrm{vl}}+\gamma_{\mathrm{vw}}A_{\mathrm{vw}}+\gamma_{\mathrm{lw}}A_{\mathrm{lw}}) \tag{26}$$

where τ is line tension, A_{vl}, A_{vw}, and A_{lw} are, respectively, the interfacial area of vapor–liquid, vapor–wall, and liquid–wall with $A_{vl}=2\pi R^2(1-\cos\theta)$ and $A_{vw}=A_{\mathrm{lw}}=\pi R^2\sin^2\theta$. Combining the total free energy, two-phase interfacial tensions as well as the modified Young's equation (Eq. 23 or 24) with Eq. 26, both the line tension and the contact angle of droplet (bubble) can be determined.

Tolman length

Tolman length indicates the extent of vapor–liquid interface tension of drop (bubble) deviating from its planar value and can be estimated by fitting $\gamma_{vl}(R)$

$$\gamma_{vl}(R)=\gamma_{vl}\left(1-\frac{2\delta}{R}\right) \tag{27}$$

where the vapor–liquid interface tension of drop (bubble) on the solid wall can be derived from the interfacial grand potential

$$\Omega_{vl}=k_{\mathrm{B}}T\sum_{i=1}^{2}\int\rho_i(\mathbf{r})[\ln(\rho_i(\mathbf{r}))-1]d\mathbf{r}+k_{\mathrm{B}}T\int\Phi^{\mathrm{hs}}[n_\alpha(\mathbf{r})]d\mathbf{r}+k_{\mathrm{B}}T\sum_{i=1}^{2}\int\rho_i(\mathbf{r})\{a[\bar{\rho}_i(\mathbf{r})]\}d\mathbf{r}-k_{\mathrm{B}}T\sum_{i=1}^{2}\int\rho_i(\mathbf{r})\mu_i d\mathbf{r} \tag{28}$$

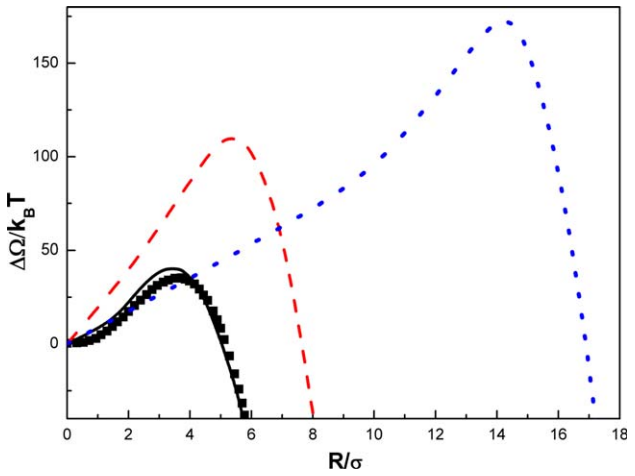

Figure 1. Constrained free energy curves of nucleation.

The solid line is calculated by 3-D-DFT for droplet nucleation of pure LJ fluid at $T^*=0.8$ and $S=2$. The squares are the corresponding simulation data.[41] The dash line is the droplet nucleation of the binary mixture and the dot line is the bubble nucleation of the binary mixture at $T^*=0.7$, $p^*=0.005$, and $S=2$ on the wall $\varepsilon_w=0.13\varepsilon$. [Color figure can be viewed in the online issue, which is available at wileyonlinelibrary.com.]

For a spherical-cap-shaped droplet (bubble), the integration volume in Eq. 28 is the product of A_{vl} and the width of vapor–liquid interface.

Results and Discussion

Heterogeneous nucleation of droplet (bubble)

The binary fluid mixture consists of component 1 and 2. In this work, σ and ε are the diameter and energy scale of component 1 and are taken as length and energy units. The parameters of component 2 are set to be $\sigma_2/\sigma=1.4$, $\varepsilon_2/\varepsilon=0.50$. The molecular diameter of the wall σ_w equals to σ, and the energy scale ε_w is given in the following for different walls. The reduced temperature and pressure of the system are fixed at $T^*=k_BT/\varepsilon=0.7$ and $p^*=p\sigma^3/\varepsilon=0.005$. In bulk system, the equilibrium vapor densities of component 1 and 2 are $\rho_1^{v*}=0.0030$ and $\rho_2^{v*}=0.0045$, respectively, and the corresponding equilibrium liquid densities are $\rho_1^{l*}=0.83$ and $\rho_2^{l*}=0.0025$, respectively.

If any one component in vapor or liquid is supersaturated, droplet or bubble nucleation could occur. As an example, Figure 1 presents a complete thermodynamic description of heterogeneous droplet or bubble nucleation on a solvophobic wall ($\varepsilon_w=0.13\varepsilon$). Without loss of generality, for droplet nucleation, we assume component 1 in vapor is supersaturated ($\rho_1^{v*}=0.0060, S=2$), a nucleated droplet emerges, and the critical nucleus radius is $R_c=5.83\sigma$. While for bubble nucleation, we assume component 2 in liquid is supersaturated ($\rho_2^{l*}=0.0050, S=2$), a nucleated bubble appears with the critical nucleus radius $R_c=14.33\sigma$. Due to different attributes of the two components, droplet and bubble nucleation are quite different. In general, bubble nucleation at

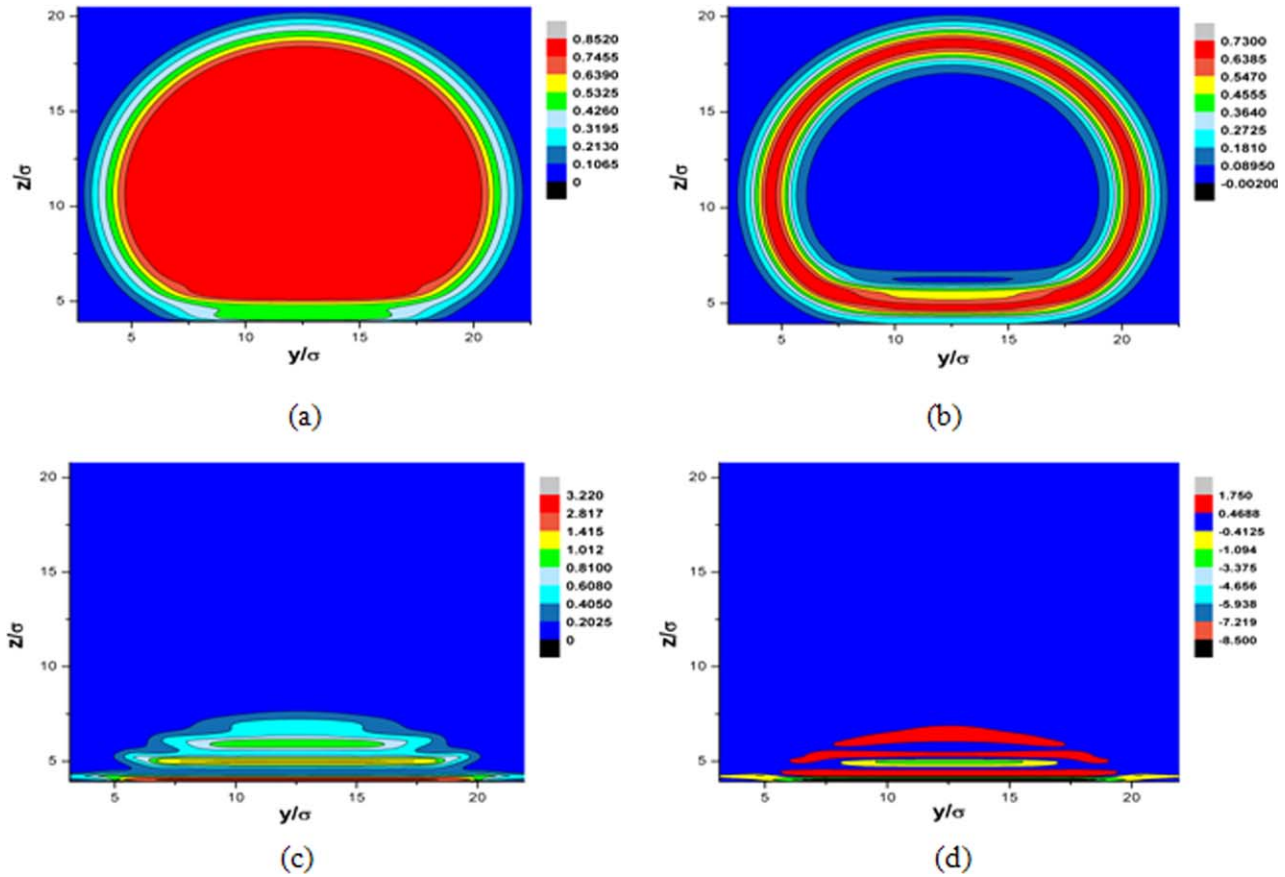

Figure 2. Two-dimensional slices of density and excess free energy configurations of droplets on different walls.

The slices are cut at $x=12.8\sigma$. (a) Density distribution of a droplet with $R=8.62\sigma$ on the wall $\varepsilon_w=0.001\varepsilon$. (b) Excess free energy distribution corresponding to (a). (c) Density distribution of a droplet with $R=10.19\sigma$ on the wall $\varepsilon_w=0.60\varepsilon$. (d) Excess free energy distribution corresponding to (c). [Color figure can be viewed in the online issue, which is available at wileyonlinelibrary.com.]

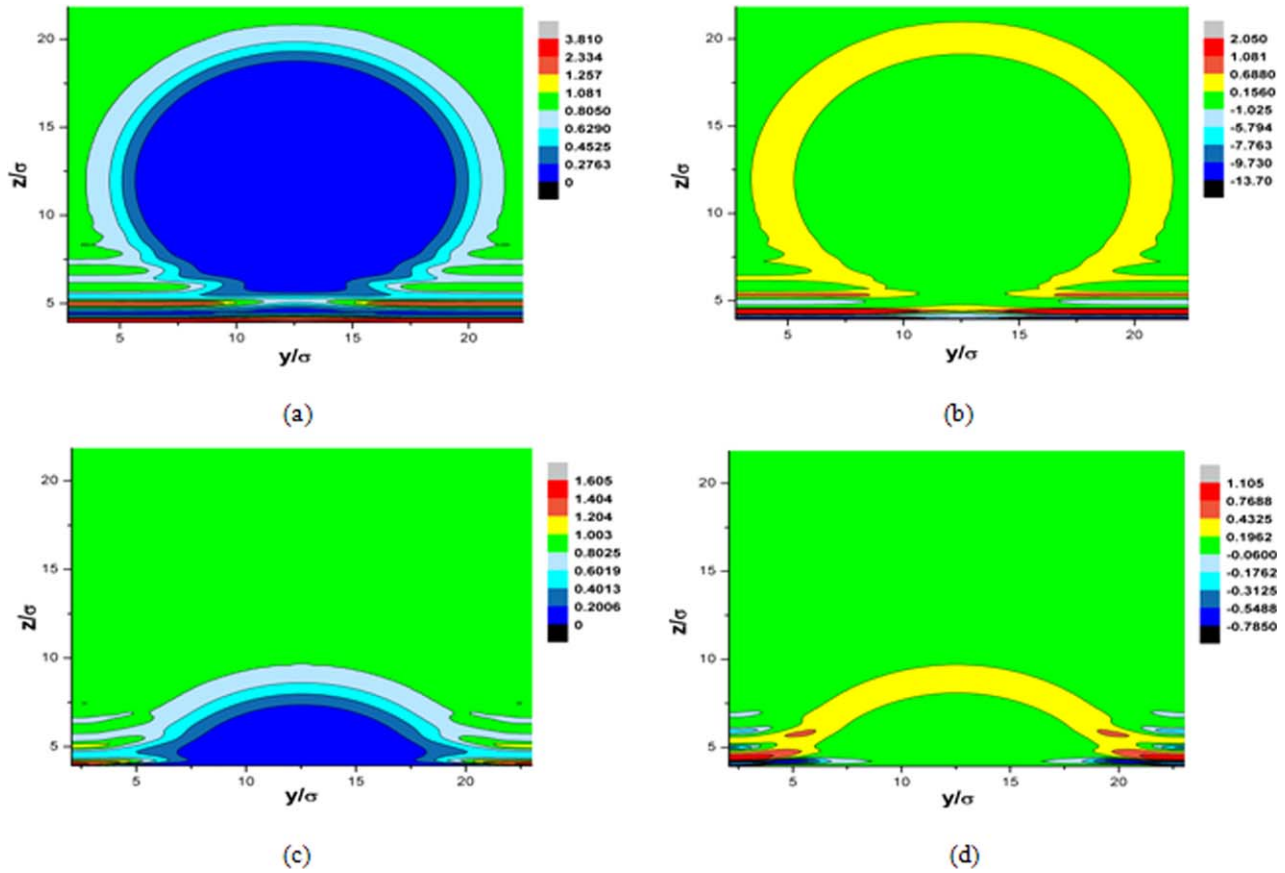

Figure 3. Two-dimensional slices of density and excess free energy configurations of bubbles on different walls.

The slices are cut at $x=12.8\sigma$. (a) Density distribution of a bubble with $R=7.35\sigma$ on the wall $\varepsilon_w=0.89\varepsilon$. (b) Excess free energy distribution corresponding to (a). (c) Density distribution of a bubble with $R=10.88\sigma$ on the wall $\varepsilon_w=0.13\varepsilon$. (d) Excess free energy distribution corresponding to (c). [Color figure can be viewed in the online issue, which is available at wileyonlinelibrary.com.]

solvophobic interface is more difficult than droplet under the same conditions, and the nucleus size of bubble is relatively large.

To test the reliability of the present 3-D model for binary fluids, Figure 1 also presents the constrained free energy of homogeneous nucleation of pure LJ fluid at $T^*=0.8$ and $S=2$, as the corresponding simulation data is available.[41] In actual calculation, the supersaturation condition is achieved through pressure variation, and the mole fractions of component 2 in both liquid and vapor phases are set to 0. In this case, the binary mixture is simplified to pure component 1, ensuring the same condition in theoretical calculation and simulation. It is shown that the calculated results are in good agreement with the simulation data, suggesting that the accuracy of the current model is acceptable.

Density and energy configurations of droplets (bubbles)

In the following discussions, the nucleation of droplet and bubble on the solid walls are analyzed under a slight supersaturation ($S=1.01$) to reduce calculation errors. Under such a supersaturation, droplets or bubbles need to grow up to a large size to form stable nuclei. While in our calculation cell, they cannot grow up to their critical nuclei, hence, they are unstable. We think that theoretical analysis of immature nuclei is reasonable as they keep the constant contact angles during their growth process.

In the present model, the contact angle of vapor–liquid–wall systems can be determined either by direct measurement or by excess free energy calculation, corresponding to the 3-D density distribution or the 3-D free energy distribution, respectively. To measure the contact angle of a droplet on solid wall, we determine those sites with $\rho \geq (\rho_l+\rho_{vs})/2$ in each layer parallel to the solid wall. Within each layer, these sites form a disk with the average radius r_{z_i}, and then the set of radii $\{r_{z_i}\}$ was fitted linearly over a set of layers of the fluid. The contact angle is the angle between this line and the solid surface.[42] For a bubble, those sites with $\rho \leq (\rho_l+\rho_{vs})/2$ are determined. Conversely, the total excess free energy of the system, as well as the interfacial tensions of vapor–liquid, vapor–wall, and liquid–wall can be derived from the 3-D free energy distributions. Accordingly, the contact angle can be calculated by combining Eq. 23 or 24 with Eq. 26.

Figure 2 presents two-dimensional (2-D) density and excess free energy distributions of droplets on different walls. In Figure 2a, at the solvophobic wall ($\varepsilon_w=0.001\varepsilon$), the measured contact angle θ_m of the bubble is 138.6°. It can be seen that, at the vapor–liquid interface and in the droplet–wall contact region, density fluctuation occurs. Inside the droplet, such fluctuation has been depressed. Corresponding to the density profile, the excess free energy distribution $\Delta F(\mathbf{r})$ is plotted in Figure 2b. Inside the droplet as well as at the vapor–liquid interface, the low-energy region correlates to the high-density region. Outside the droplet, the excess free energy declines to zero. While at solvophilic wall ($\varepsilon_w=0.60\varepsilon$), the density (Figure 2c) and excess free energy (Figure 2d) of the droplet display significantly layered

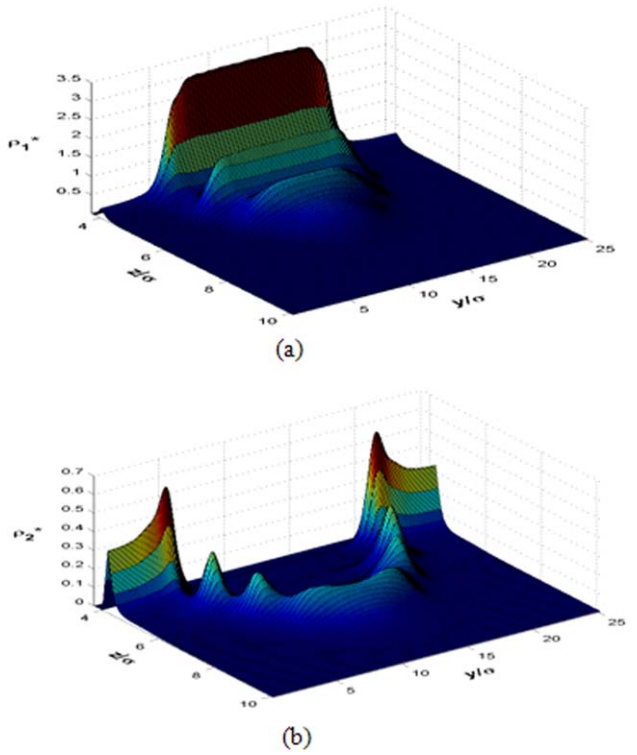

Figure 4. Two-dimensional density profiles of component 1 (a) and 2 (b) of the droplet in Figure 2c.

[Color figure can be viewed in the online issue, which is available at wileyonlinelibrary.com.]

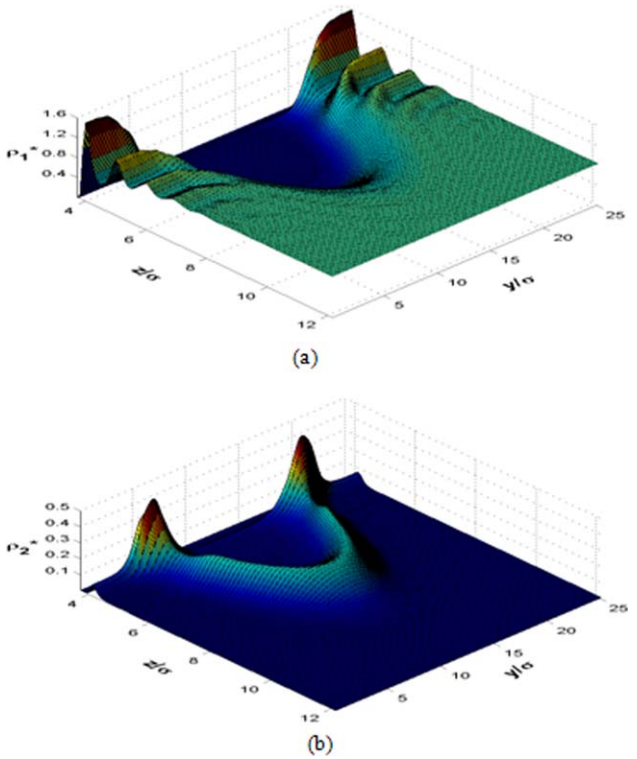

Figure 5. Two-dimensional density profiles of component 1 (a) and 2 (b) of the bubble in Figure 3c.

[Color figure can be viewed in the online issue, which is available at wileyonlinelibrary.com.]

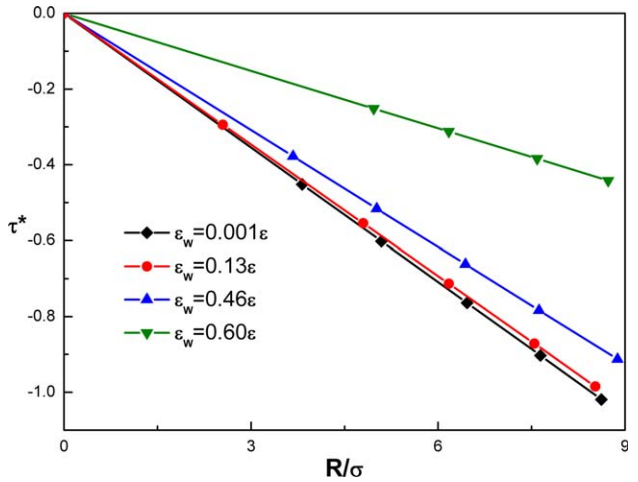

Figure 6. Line tension as a function of droplet radius on different walls.

[Color figure can be viewed in the online issue, which is available at wileyonlinelibrary.com.]

distributions, the measured contact angle θ_m is 45.5°. Similar to Figure 2b, the low-energy region corresponds to the high-density region. Once the free energy distribution has been determined, the total excess energy of droplet can be easily obtained.

Figure 3 shows the density and excess free energy distributions of bubbles near solvophilic ($\varepsilon_w=0.89\varepsilon$) and solvophobic ($\varepsilon_w=0.13\varepsilon$) walls, respectively. Near the solvophilic wall, one sees that density fluctuation (Figure 3a) emerges at the vapor–liquid interface and in the vicinity of wall. In particular, a liquid film can be observed between bubble and wall. Due to the strong solvophilic attribute of the wall, liquid cannot be depleted entirely by the nucleated bubble. Inside the bubble, the densities are almost uniform. The measured contact angle θ_m is 155.6°. Similarly, the excess free energy (Figure 3b) fluctuation is opposite to the density fluctuation. Near the solvophobic wall, a pancake bubble emerges. The density and energy distributions are plotted in Figures 3c and 3d, respectively. The measured contact angle

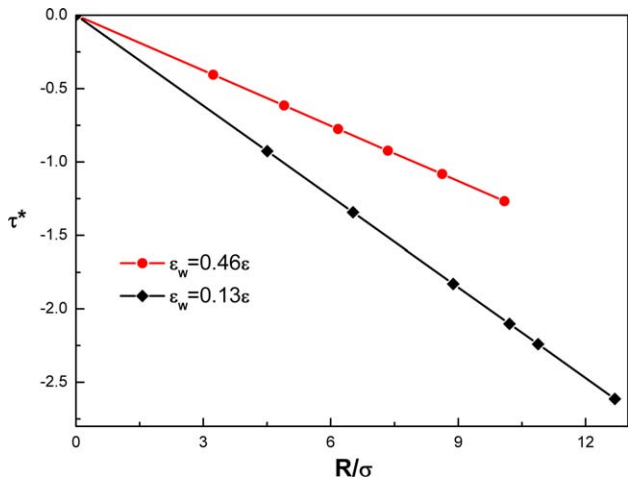

Figure 7. Line tension as a function of bubble radius on different walls.

[Color figure can be viewed in the online issue, which is available at wileyonlinelibrary.com.]

Table 1. Comparison of Measured and Calculated Contact Angles

	ε_w	Measured Value θ_m	Calculated Value Without Line Tension θ	Relative Deviation ($\lvert\theta-\theta_m\rvert/\theta_m \times 100\%$)	Calculated Value with Line Tension θ_c	Relative Deviation ($\lvert\theta_c-\theta_m\rvert/\theta_m \times 100\%$)
Droplet	0.001	138.6	147.8	6.63	131.4	5.19
	0.13	104.4	112.3	7.60	103.9	0.48
	0.46	60.6	68.5	13.0	60.2	0.66
	0.60	45.5	52.8	16.0	46.6	2.40
Bubble	0.13	41.9	67.7	61.6	35.3	15.8
	0.46	107.2	111.5	4.01	103.0	3.92

θ_m is 41.9°. Due to the relatively weak solvophility of the wall, no liquid film can be seen in Figure 3c.

In order to clearly observe the density distributions of different components during droplets or bubbles nucleation, the density profiles of components 1 and 2 are, respectively, provided. Figure 4 shows the density profiles of components 1 and 2 of the droplet nucleus in Figure 2c. In Figure 4a, component 1 display three peaks inside the droplet. The first peak is the highest and appears at σ from the solid wall ($z=4\sigma$), and successive peaks arise at intervals of σ. For the component 2 (Figure 4b), the density inside the droplet keep at low level. Along the edge of the droplet, the first peak emerges at 1.4σ from the solid wall ($z=4.4\sigma$) and the successive ones occur at intervals of σ. The location of the first peak of component 2 is determined by its molecular size. In the vicinity of wall, the maximum adsorption of component 1 is lower than that of component 2. This is because that, in bulk vapor, the content of component 2 is slightly higher.

Figure 5 shows the density distribution of each component of the bubble in Figure 3c. Inside the bubble, the densities of both components are nearly uniform. Outside the bubble, the layered distribution of component 1 is aroused by the adsorption of the liquid. For component 2, there is only a peak near the wall. In addition, there exists an enrichment of component 2 at the vapor–liquid interface.

Determination of line tension and contact angle

To confirm the role of line tension in heterogeneous nucleation, we analyze the energy and the force balance along the three-phase contact line. Accordingly, the line tensions are calculated and plotted in Figure 6 for droplet and Figure 7 for bubble, respectively. The results show that the line tensions for droplets and bubbles are negative. As the droplet or bubble radius increases, the line tension declines linearly, implying that line tension becomes more pronounced for larger droplet or bubble. As the solvophobicity of wall increases, the absolute value of the line tensions increases, but the growth rate shrinks. Meanwhile, the contact angles of droplet and bubble are also obtained. The results are listed in Table 1. For comparison, the measured values and the calculated ones without consideration of line tension are also given in the table. For droplets, the calculated contact angles with the line tension correction coincide well with the measured data, whereas those calculated values without the

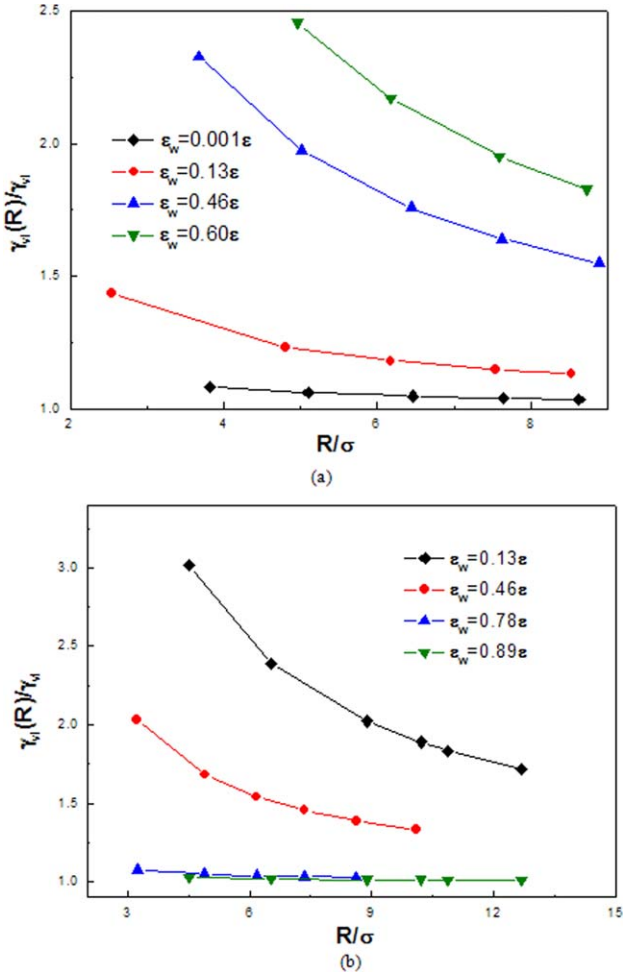

Figure 8. Relative interface tension as a function of nucleus radius on different walls.

(a) Droplet and (b) bubble. Here, γ_{vl} is the planar interface tension. [Color figure can be viewed in the online issue, which is available at wileyonlinelibrary.com.]

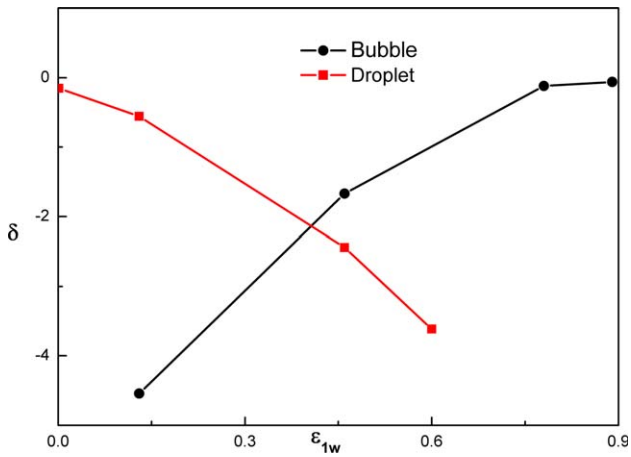

Figure 9. Tolman lengths of droplets and bubbles as a function of wall solvophilicity. [Color figure can be viewed in the online issue, which is available at wileyonlinelibrary.com.]

correlation deviate from the measured ones systematically, and the error increases quickly as the wall solvophilicity increases. For bubbles, the calculated values including the line tension correction are much better than the ones without the correction.

Tolman length

Due to the curvature of vapor–liquid interface, the interface tensions of droplets (bubbles) deviate from the planar value. Figure 8 shows the curved interface tension $\gamma_{vl}(R)$ of droplets (Figure 8a) and bubbles (Figure 8b), respectively. One sees that $\gamma_{vl}(R)$ of droplets decreases with the increasing nucleus radius or wall solvophobicity, $\gamma_{vl}(R)$ of bubble decreases with the increasing nucleus radius or wall solvophilicity.

By fitting $\gamma_{vl}(R)$, Tolman lengths of droplets and bubbles are obtained and given in Figure 9. It is shown that Tolman lengths are always negative during the droplet and bubble nucleation process. For droplets, as the solvophilicity increases, Tolman length decreases. Tolman length approaches to zero at supersolvophobicity wall, meaning that the first-order correction to the interface tension is insignificant. While for bubbles, Tolman length increases up to zero with the increasing solvophilicity.

Conclusions

The effect of line tension on the contact angle has been investigated in heterogeneous droplet (bubble) nucleation of binary LJ fluid using a 3-D-DFT model. We note that no mixing parameter is introduced into the model. The accuracy of the theoretical approach has been tested with simulation data for homogenous nucleation of pure fluid. The density and excess free energy distributions of droplets and bubbles on solvophilic and solvophobic walls have been systematically investigated and presented. More importantly, the line tensions and contact angles have been determined based on the corresponding total excess energy. The results show that, during heterogeneous droplet (bubble) nucleation, the line tensions are negative, and the absolute values increase as the solvophobicity of wall increases. Meanwhile, these contact angles have also been measured directly from the spatial density configurations. With these line tensions, the calculated contact angles have been distinctly modified. In addition, Tolman lengths for droplet and bubble are calculated and analyzed.

Acknowledgments

This work is supported by National Natural Science Foundation of China (No. 21076006) and by Chemcloudcomputing of Beijing University of Chemical Technology.

Literature Cited

1. Drossions Y, Kevrekidis PG. Classical nucleation theory revisited. *Phys Rev E*. 2003;67:026127.
2. Kashchiev D. Nucleation: Basic Theory with Applications. Oxford: Butterworth-Heinemann, 2000.
3. Iland K, Wolk J, Strey R, Kashchiev D. Argon nucleation in a cryogenic nucleation pulse chamber. *J Chem Phys*. 2007;127:154506.
4. Wedekind J, Hyvarinen AP, Brus D, Reguera D. Unraveling the "pressure effect" in nucleation. *Phys Rev Lett*. 2008;101:125703.
5. Carreon-Calderon B, Soria A, Romero-Martinez A. Driving force in first-order phase transitions and its application to gas hydrate nucleation from a single phase. *AIChE J*. 2009;55:2433–2447.
6. Talanquer V, Oxtoby DW. Nucleation on a solid substrate: a density functional approach. *J Chem Phys*. 1996;104:1483–1492.
7. Das SK, Binder K. Simulation of binary fluids exposed to selectively adsorbing walls: a method to estimate contact angles and line tensions. *Mol Phys*. 2011;109:1043–1056.
8. Eslami F, Elliott JAW. Thermodynamic investigation of the barrier for heterogeneous nucleation on a fluid surface in comparison with a rigid surface. *J Phys Chem B*. 2011;115:10646–10653.
9. Iwamatsu M. Heterogeneous critical nucleation on a completely wettable substrate. *J Chem Phys*. 2011;134:234709.
10. Fsadni AM, Ge YT, Lamers AG. Bubble nucleation on the surface of the primary heat exchanger in a domestic central heating system. *Appl Therm Eng*. 2012;45–46:24–32.
11. Bykov TV, Zeng XC. Homogeneous nucleation at high supersaturation and heterogeneous nucleation on microscopic wettable particles: a hybrid thermodynamic/density-functional theory. *J Chem Phys*. 2006;125:144515.
12. Winkler PM, Hienola A, Steiner G, Hill G, Vrtala A, Reischl GP, Kulmala M, Wagner PE. Effects of seed particle size and composition on heterogeneous nucleation of n-nonane. *Atmos Res*. 2008;90:187–194.
13. Turnbull D. Kinetics of heterogeneous nucleation. *J Chem Phys*. 1950;18:198–203.
14. Verdaguer A, Sacha GM, Bluhm H, Salmeron M. Molecular structure of water at interfaces: wetting at the nanometer scale. *Chem Rev*. 2006;106:1478–1510.
15. Aveyard R, Clint JH, Nees D. Theory for the determination of line tension from capillary condensation. *J Chem Soc Faraday Trans*.1997;93:4409–4411.
16. Gokhale SJ, Plawsky JL, Wayner Jr PC. Effect of interfacial phenomena on dewetting in dropwise condensation. *Adv Colloid Interface Sci*. 2003;104:175–190.
17. Weijs JH, Marchand A, Andreotti B, Lohse D, Snoeijer JH. Origin of line tension for a Lennard-Jones nanodroplet. *Phys Fluids*. 2011;23:022001.
18. Amirfazli A, Neumann AW. Status of the three-phase line tension. *Adv Colloid Interface Sci*. 2004;110:121–141.
19. Rusanov AI. Surface thermodynamics revisited. *Surf Sci Rep*. 2005;58:111–239.
20. Greer AL. Triple lines in nucleation. *Scr Mater*. 2010;62:899–903.
21. Asekomhe SO, Elliott JAW. The effect of interface deformation due to gravity on line tension measurement by the capillary rise in a conical tube. *Colloids Surf A*. 2003;220:271–278.
22. Amirfazli A, Keshavarz A, Zhang L, Neumann AW. Determination of line tension for systems near wetting. *J Colloid Interface Sci*. 2003;265:152–160.
23. Bresme F, Oettel M. Nanoparticles at fluid interfaces. *J Phys: Condens Matter*. 2007;19:413101.
24. Marmur A. Line tension and the intrinsic contact angle in solid–liquid–fluid systems. *J Colloid Interface Sci*. 1997;186:462–466.
25. Marmur A, Krasovitski B. Line tension on curved surfaces: liquid drops on solid micro- and nanospheres. *Langmuir*. 2002;18:8919–8923.
26. Djikaev Y, Widom B. Geometric view of the thermodynamics of adsorption at a line of three-phase contact. *J Chem Phys*. 2004;121:5602–5610.
27. Widom B. Models of adsorption at a line of three-phase contact. *J Phys Chem B*. 2006;110:22125–22132.
28. Schimmele L, Napiorkowski M. Conceptual aspects of line tensions. *J Chem Phys*. 2007;127:164715.
29. Indekeu JO, Koga K, Widom B. How much does the core structure of a three-phase contact line contribute to the line tension near a wetting transition? *J Phys: Condens Matter*. 2011;23:194101.
30. Mi JG, He YJ, Zhong CL. Theoretical study of wetting behavior of nanoparticles at fluid interfaces. *AIChE J*. 2009;55:747–755.
31. Zeng M, Mi JG, Zhong CL. Wetting behavior of spherical nanoparticles at a vapor–liquid interface: a density functional theory study. *Phys Chem Chem Phys*. 2011;13:3932–3941.
32. Zhou D, Mi JG, Zhong CL. Three-dimensional density functional study of heterogeneous nucleation of droplets on solid surfaces. *J Phys Chem B*. 2012;116:14100–14106.
33. Knepley MG, Karpeev DA, Davidovits S, Eisenberg RS, Gillespie D. An efficient algorithm for classical density functional theory in three dimensions: ionic solutions. *J Chem Phys*. 2010;132:124101.
34. Trudeau TG, Jena KC, Hore DK. Water structure at solid surfaces of varying hydrophobicity. *J Phys Chem C*. 2009;113:20002–20008.

35. Yu Y-X, Wu JZ. Structures of hard-sphere fluids from a modified fundamental-measure theory. *J Chem Phys*. 2002;117:10156–10164.
36. Barker JA, Henderson D. Perturbation theory and equation of state for fluids. II. A successful theory of liquids. *J Chem Phys*. 1967;47:4714–4721.
37. Leidl R, Wagner H. Hybrid WDA: a weighted-density approximation for inhomogeneous fluids. *J Chem Phys*. 1993;98:4142–4148.
38. Tang YP. A SAFT model for associating Lennard-Jones chain mixtures. *Mol Phys*. 2002;100:1033–1047.
39. Tang YP, Wu JZ. Modeling inhomogeneous van der Waals fluids using an analytical direct correlation function. *Phys Rev E*. 2004;70:011201.
40. Drelich J. The significance and magnitude of the line tension in three-phase (solid–liquid–fluid) systems. *Colloids Surf A: Physicochem Eng Asp*. 1996;116:43–54.
41. Moody MP, Attard P. Curvature-dependent surface tension of a growing droplet. *Phys Rev Lett*. 2003;91:056104.
42. Porcheron F, Monson PA. Mean-field theory of liquid droplets on roughened solid surfaces: application to superhydrophobicity. *Langmuir*. 2006;22:1595–1601.

Manuscript Received Feb. 6, 2013 and revision received April 9, 2013.